Mitochondrial cristae biogenesis coordinates with ETC complex IV assembly during *Drosophila* maturation

*Yi-fan Jiang[1], Hsiang-ling Lin[2], Li-jie Wang[2], Tian-Hsu[2], and Chi-yu Fu[2]**

[1]*Graduate Institute of Molecular and Comparative Pathobiology, School of Veterinary Medicine, National Taiwan University, Taipei, Taiwan*

[2]*Institute of Cellular and Organismic Biology, Academia Sinica, Taipei, Taiwan*

Abstract

Mitochondrial cristae contain electron transport chain (ETC) complexes and are distinct from the inner boundary membrane (IBM) in both protein composition and function. While many details of mitochondrial membrane structure are known, the processes governing cristae biogenesis, including the organization of lipid membranes and assembly of proteins encoded by both nuclear and mitochondrial DNA, remain obscure. We followed cristae biogenesis *in situ* upon *Drosophila* eclosion using serial-section electron tomography and revealed that the morphogenesis of lamellar cristae coordinates with ETC complex IV assembly. The membrane morphogenesis and gain-of-function were intricately co-evolved during cristae biogenesis. Marf-knockdown flies formed lamellar cristae containing ATP synthase and functional COX. However, OPA1-knockdown flies showed impaired cristae biogenesis. Overall, this study revealed the multilevel coordination of protein-coupled membrane morphogenesis in building functional cristae.

Key words: mitochondria/ cristae biogenesis/ COX assembly/ membrane morphogenesis/ electron tomography

Running title: Mitochondrial cristae biogenesis

Introduction

Mitochondria originate from an endosymbiosis event. The organelles exhibit unique double membrane architecture, consisting of outer and inner membranes that are separated by an intermembrane space. The inner membrane can be further subdivided into the inner boundary membrane (IBM) and the cristae invaginations, based on the ultrastructure, protein composition and function (Cogliati, Enriquez et al., 2016, Mannella, 2006). In the cristae, electron transport chain (ETC) complexes generate ATP by creating and maintaining a proton gradient between the matrix and intermembrane space (Gilkerson, Selker et al., 2003). Importantly, the morphology and remodeling of cristae are indicative of mitochondrial function, and cristae ultrastructure is known to be heavily influenced by several critical proteins (Cogliati, Frezza et al., 2013, Frezza, Cipolat et al., 2006, Scorrano, Ashiya et al., 2002). For example, ATP synthase has been shown to play a structural role in inducing positive membrane curvature at the cristae ridges in addition to its enzymatic function (Davies,

Strauss et al., 2011, Strauss, Hofhaus et al., 2008). Secondly, the mitochondrial contact site and cristae organizing system (MICOS) complex is known to stabilize the cristae junction, the region where cristae connect to the IBM (Huynen, Muhlmeister et al., 2016, Rampelt, Zerbes et al., 2017, Schorr & van der Laan, 2017). Optic atrophy protein 1 (OPA1), a protein involved in inner membrane fusion, also plays a pivotal role in stabilizing cristae junctions and mediating cristae remodeling during apoptosis (MacVicar & Langer, 2016, Varanita, Soriano et al., 2015). Even though key proteins have been identified as being essential for the maintenance and the remodeling of cristae architecture, the question of how functional cristae form *de nov*o, including the organization of lipid membranes and assembly of proteins encoded by both nuclear and mitochondrial DNA, remains to be elucidated.

In this study, we investigated the mechanisms of cristae biogenesis by characterizing the mitochondrial development of *Drosophila* upon eclosion, the emergence of adult flies from pupa. At larval and pupal stages, *Drosophila* uses aerobic glycolysis to support the rapid growth of body mass and subsequent metamorphosis (Agrell, 1953, Tennessen, Baker et al., 2011). Upon eclosion, mitochondrial cristae undergo development to support increased energy demand. During this time, mature mitochondria in the indirect flight muscle (IFM) establish densely arranged lamellar cristae that form connective membrane networks (Jiang, Lin et al., 2017b), providing a well-characterized physiological time reference for the *de novo* formation of functional cristae. Using this model system, we were able to uncover novel mechanisms of cristae biogenesis that involve intricate coordination of membrane morphogenesis and ETC complex IV assembly.

Results

Mitochondria exhibit cristae biogenesis upon *Drosophila* eclosion

To characterize mitochondrial structure in *Drosophila* during eclosion from the pupa, the IFM of adult flies was sampled at various time points. Thin-section TEM analysis showed that the mitochondria at day 1 after eclosion contained only a few organized cristae that were loosely scattered throughout the matrix (Fig 1a). The mitochondria developed densely packed lamellar cristae, usually within a couple days, as what was observed in the matured flies (Fig 1b) (Jiang et al., 2017b). The mitochondrial protein abundance during maturation was analyzed. The mitochondria of day 1 flies contained a low level of ATP5A (complex V of the ETC complex) compared to those of the week 4 flies according to the immuno-EM (Fig 2a-b). The western blots analysis of the whole fly extracts showed that at day 1, some other nuclear DNA-encoded mitochondrial proteins, such as pyruvate dehydrogenase (PDHA1), superoxide dismutase 2 (SOD2), and Cytochrome c (Cyt c), were approximately 30-50% of the levels in the week 4 flies (Fig 2c). On the other hand, the ribosomal protein, RPS6, was expressed roughly 18-fold more in the day 1 flies than week 4 flies (Fig 2c). Consistent with this observation, thin-section TEM

micrographs revealed highly abundant ribosome or polyribosome-like structures in the cytoplasm of day 1 flies, but these structures were much less abundant in the week 4 flies (Fig 1a-b). With this reliably orchestrated transition in mitochondrial morphology, the eclosion of *Drosophila* provides an excellent model system with which to elucidate the development of cristae ultrastructure and function *in situ*.

To track cristae organization during mitochondrial maturation in 3D, we applied serial section electron tomography to reconstruct entire mitochondrial volumes. The global organization of IFM tissue was established upon eclosion with mitochondria distributed between parallel muscle fibers. In some cases, close inter-mitochondrial contacts were already observed, which may facilitate communication between mitochondria (Fig 1c-d, Movie 1) (Picard, McManus et al., 2015). Mitochondria in the day 1 flies appeared more polymorphic and contained lamellipodia-like or filopodia-like extensions, which became ovoid-shaped and filled the cytoplasmic space between the muscle fibers as they matured (Movie 1). Concentrated cytoplasmic ribosome or polyribosome-like densities surrounded the immature mitochondria, which would be expected to support rapid protein synthesis for mitochondria maturation (Fig 1c-d). A cryo-tomography study reported that cytoplasmic ribosomes associate with the mitochondrial surface through the interaction with TOM complex (Gold, Chroscicki et al., 2017).

Joined serial tomograms of the day 1 flies showed that the mitochondrial matrix also contained numerous darkly stained ribosome-like molecules along with the segments of lamellar cristae (Fig 1c-d, Movie 1). In the mature mitochondria, mitochondrial ribosomes cannot be not readily observed in the densely confined matrix compartment. Due to the lack of available antibodies against *Drosophila* mitochondrial ribosome, the change of mitochondrial ribosome level during maturation cannot be quantified.

Cristae biogenesis coordinates with COX complex assembly

Functional cristae require the proper organization of membrane and protein assembly. To investigate whether membrane morphogenesis of the cristae correlates with the assembly of ETC complexes, we applied Cytochrome c oxidase (COX) staining to visualize COX activity in the context of the ultrastructure. COX oxidizes 3,3′-diaminobenzidine (DAB) and forms osmiophilic precipitants in the presence of osmium tetraoxide that appear darkly stained under TEM. The osmium tetraoxide substrate also binds to the head group of phospholipids that creates weak contrast for lipid membranes.

Mitochondria of the day 1 flies exhibited some lamellae of cristae with prominent COX activity, while vesicular membranous structures that filled the mitochondrial matrix had weak staining (Fig 3a-b). To characterize their 3D arrangement, serial section electron tomography was applied. In the whole-mitochondria reconstructions, mostly isolated segments of lamellar cristae

were observed scattered throughout the matrix (Fig 3c-e, Movie 2). Tomographic reconstructions also revealed that the vesicular membranous structures in the matrix actually formed a reticulum-like organization in 3D (Fig 3c-e). We defined them as the reticular membrane and did not use the word "cristae," as they contained very limited COX activity. The reticular membranes appeared to merge with the ends of lamellar cristae and gained COX activity as the membrane became organized as a part of the lamellae with a more defined width (Fig 3c-d, Movie 2).

We also generated a knockin fly that expresses Apex2 conjugated to the c-terminus of COX4, which is a subunit of COX that is synthesized in the cytoplasm and subsequently transported into the mitochondria (Fig S1a-b). Apex2, an ascorbate peroxidase, catalyzes the polymerization of DAB in the presence of hydrogen peroxide (H_2O_2), which enhances EM contrast after osmium tetraoxide staining, thus allowing us to track COX4 protein localization at the ultrastructural level (Martell, Deerinck et al., 2012). Using this method, COX4 was shown to localize mainly to the organized lamellar cristae in the day 1 flies, which correlated with the COX activity staining data (Fig 4a). The wild type flies were performed as the negative control of the Apex2 staining (Fig 4b). According to the structural studies, the c-terminus of COX4 is apposed to the intermembrane space, where the Apex2 staining appeared (Fig 4a) (Wu, Gu et al., 2016).

The COX complex comprises multiple subunits encoded by both nuclear and mitochondrial DNA. The insertion and assembly of the COX complex subunits require OXA1, which mediates the insertion of both nuclear and mitochondrial DNA-encoded polypeptides from the matrix into the inner membrane (Keil, Bareth et al., 2012, Soto, Fontanesi et al., 2012). OXA1 was shown to present in IBM and cristae in yeast by immuno-gold EM study (Stoldt, Wenzel et al., 2012). We set out to visualize if OXA1 also locates in the cristae to facilitate COX assembly during mitochondrial maturation in *Drosophila*. We tracked OXA1 localization in OXA1-Apex2 knockin flies at higher spatial resolution using the Apex2 method. Indeed Apex2 staining was present in the cristae and the IBM (Fig 4c, S1a). The negative control of the Apex2 staining using the wild type flies was shown in Fig 3d. Judging by the staining location, the c-terminal Apex2 tag faced the matrix side of the inner membrane, and the staining pattern appeared as granular densities (Fig 4c). The result was also confirmed in S2 cells that over-expressed OXA1-Apex2 (Fig 4e). The cells with mock-transfection were used as the negative control of Apex2 staining (Fig 4f). The western-blot of OXA1-Apex2 expression in S2 cells was shown in Fig S1c.

The data showed lamellar cristae are organized in coordination with the assembly of COX during cristae biogenesis upon *Drosophila* eclosion. The study revealed the intricate coordination of membrane morphogenesis and gain-of-function.

Marf-knockdown flies formed lamellar cristae containing ATP synthase and functional COX

Marf, a homolog of human mitofusin 1 and 2, mediates outer membrane fusion and influences ER-mitochondria tethering (de Brito & Scorrano, 2008, Detmer & Chan, 2007, Filadi, Greotti et al., 2015, Filadi, Pendin et al., 2018, Schrepfer & Scorrano, 2016). To investigate how Marf affects cristae biogenesis and mitochondrial maturation, we investigated the mitochondrial structure and function of Marf-knockdown flies. Marf-knockdown flies had compromised climbing ability but had similar expression levels of ATP5A, PDHA1, SOD2 and Cyt c in the whole fly extracts, compared to the wild type flies (Fig S2a, b). Thin-section TEM and serial-section tomography revealed that lamellar cristae were formed in Marf-knockdown mitochondria (Fig 5a-d, Fig S2c-d, Movie 3). In addition, they had normal COX activity (Fig 5e), as well as ATP5A and Cyt c shown by the immuno-EM (Fig 5f, Fig S2f). The Apex2 staining of the ATP synthase OSCP-Apex2 knockin flies in the Marf-knockdown background also confirmed the presence of ATP synthase OSCP in the cristae (Fig 5g, Fig S2h). The dark staining of OSCP-Apex2 was restricted to the matrix side of the cristae. It correlated with the structural studies of properly assembled ATP synthase and suggested correct folding and targeting of OSCP-Apex2 in the knockin flies (Fig 5g) (Wu et al., 2016, Zhou, Rohou et al., 2015). The data showed the formation of functional cristae was not impaired in Marf-knockdown flies.

However, Marf-knockdown mitochondria were approximately 49% smaller than the wild type, which was expected given that mitochondrial outer membrane fusion was impaired. In addition, the cristae content per mitochondrial volume was reduced to approximately 53% in the Marf-knockdown flies, comparing to approximately 99% in the wild type at week 4. This observation probably reflects the alteration of ER-mitochondria tethering in the Marf-knockdown, which is essential for lipid transport to the mitochondria from the ER (Area-Gomez, Del Carmen Lara Castillo et al., 2012, Filadi et al., 2018, Tatsuta & Langer, 2017, Vance, 2014).

OPA1-knockdown flies showed impaired cristae biogenesis

We investigated how OPA1 affects mitochondrial maturation and cristae biogenesis. OPA1-knockdown flies showed reduced climbing ability, even though several nuclear DNA-encoded mitochondrial proteins were expressed at a similar level as in the wild type flies in the whole fly extracts (Fig S3a-b). OPA1-knockdown mitochondria were approximately 42% smaller than the wild type mitochondria, as a result of defective mitochondrial fusion. Many mitochondria contained very few organized membranes but vacuoles, some likely resulting from the incomplete inner membrane fusion post the outer membrane fusion (Fig 6a, Fig S3c). Most OPA1-knockdown mitochondria had disordered and aberrant membranes.

OPA1-knockdown mitochondria also had very low levels of functional COX assemblies in both day 1 and week 4 flies (Fig 6b, f, Fig S3d, Movie 4). Only about 5% of the mitochondria exhibited positive COX staining. Even though western-blot of

206 the whole fly extracts showed some mitochondrial proteins were at a similar level in
207 the OPA1-knockdown as in the wild type, immuno-EM showed a reduced level of
208 ATP5A (F_1 subunit α) and cytochrome c proteins in OPA1-knockdown mitochondria
209 (Fig 6c, Fig S3e-h). In correlation, ATP synthase OSCP-Apex2 knockin conjugates
210 under OPA1-knockdown background only appeared in a few regional lamellar
211 membranes (Fig 6d). Dysmorphic cristae ultrastructure and decreased ETC assemblies
212 likely led to a vicious circle of low membrane potential and impaired protein transport
213 (Harbauer, Zahedi et al., 2014, Song, Chen et al., 2007). OPA1 was also shown to
214 affect mitochondrial DNA maintenance that likely contributed to the ill mitochondrial
215 function and morphogenesis (Elachouri, Vidoni et al., 2011).
216 We tracked OPA1 localization by Apex2 conjugation in 293T cells
217 overexpressing human OPA1-Apex2 (Fig 6e, S4a-b), as well as in S2 cells
218 overexpressing *Drosophila* OPA1-Apex2 (Fig S4c-d). OPA1 protein was observed in
219 both cristae and the IBM. Opa1-Apex2 knockin flies had very low expression of
220 OPA1-Apex2, approximately 7% of the expression of COX4-Apex2 knockin by
221 western blot against Flag tag (Fig S1a, S4e-f). The physical localization of OPA1
222 correlates with its role in mediating inner membrane fusion or cristae remodeling.
223
224 **Discussion**
225 In this study, we took the advantage of *Drosophila* model that displayed
226 dramatic cristae biogenesis upon eclosion in building compact lamellar cristae. We
227 showed that the development of cristae morphology and function is intricately
228 coordinated. Most mitochondrial lipids or the precursors are imported from ER
229 through the proteins mediating membrane contacts and lipid translocation (Flis &
230 Daum, 2013, Tatsuta & Langer, 2017). One mechanism of cristae formation was
231 proposed as through the invagination of IBM (Harner, Unger et al., 2016). The COX
232 complex is composed of subunits encoded by both nuclear and mitochondrial DNA.
233 The assembly pathway has been described in great detail and involves the
234 coordination of multiple steps, including protein synthesis, membrane insertion,
235 assembly, and metal incorporation, all of which are mediated by various chaperones
236 and accessory proteins (Soto et al., 2012). In our study, we showed at a high spatial
237 resolution that OXA1 insertase localizes in the cristae as well as the IBM, where it
238 may assist in COX assembly. Mitochondrial cristae morphology was shown to
239 determine the ETC supercomplex assembly and respiratory efficiency (Cogliati et al.,
240 2013). Our study uncovered an extra layer of coordination between the assembly of
241 COX and the establishment of initial cristae ultrastructure.
242 Marf is a homolog of human mitofusin 1 and mitofusin 2. It plays important role
243 in mitochondrial outer membrane fusion, ER-mitochondria interaction, and
244 neuromuscular function (de Brito & Scorrano, 2008, Detmer & Chan, 2007, Filadi et
245 al., 2015, Filadi et al., 2018, Khalil, Cabirol-Pol et al., 2017, Sandoval, Yao et al.,
246 2014, Schrepfer & Scorrano, 2016). We showed that Marf-knockdown flies formed

247 lamellar cristae containing ATP synthase and functional COX but with reduced size.
248 In previous studies, Marf-knockdown was also shown to have normal cristae
249 morphology, ETC supercomplex assembly, but decrease mtDNA copy number
250 (Cogliati et al., 2013).
251 OPA1-knockdown flies had impaired cristae morphogenesis, likely reflects its
252 essential role in various aspects of mitochondrial processes. OPA1, a dynamin-related
253 GTPase, is anchored in the inner membrane in its long isoform. Upon proteolytic
254 cleavage, the short isoform becomes localized to the intermembrane space. This
255 proteolysis-mediated redistribution is an important regulatory mechanism in
256 OPA1-mediated membrane fusion and fission (Ban, Ishihara et al., 2017, Del Dotto,
257 Mishra et al., 2017, MacVicar & Langer, 2016). OPA1 has also been shown to control
258 cristae remodeling and junction widening during apoptosis (Frezza et al., 2006). It
259 was shown to protect mitochondria from complex III inhibition by stabilizing cristae
260 morphology and ATP synthase oligomers (Quintana-Cabrera, Quirin et al., 2018). In
261 this study, we showed the physical localization of OPA1 in the ultrastructure that
262 allows its dual role in cristae remodeling and inner membrane fusion.
263 Through evolution, mitochondria have been delicately integrated as organelles,
264 which contain highly functionalized compartments and membranes. Thus, it is no
265 surprise that a sophisticated biomolecular interaction network is being uncovered in
266 the regulation of cristae architecture (Jayashankar, Mueller et al., 2016). As part of
267 this network, OPA1 was previously shown to interact with MIC60 of the MICOS
268 complex in the cristae and cristae junction (Hoppins, Collins et al., 2011, Sastri,
269 Darshi et al., 2017). Furthermore, the lipid, cardiolipin, was shown to stabilize ETC
270 components and shape cristae architecture (Desmurs, Foti et al., 2015, Paradies,
271 Paradies et al., 2014). Here we demonstrated the intricate multilevel coordination of
272 building functional cristae. In the study, the generalized mechanism of
273 protein-coupled membrane morphogenesis was clearly demonstrated for cristae
274 biogenesis, which is in line with various other membrane remodeling processes, such
275 as vesicle budding and fusion (Bonifacino & Glick, 2004).
276
277
278 **Materials and Methods**
279 ***Fly strains***
280 *Drosophila* strains on the Oregon-R-P2 background were used in these studies.
281 Marf-knockdown flies were obtained by crossing UAS (Bloomington 31157) and
282 GAL4 (Bloomington 26882) lines. OPA1-knockdown flies were obtained by crossing
283 UAS (Bloomington 32358) and GAL4 (Bloomington 38459) lines.
284 Apex2-Flag knockin flies of COX4, OXA1, ATP synthase OSCP, and OPA1
285 were generated by CRISPR/Cas9-mediated genome editing and homology-dependent
286 repair using a guide RNA(s) and a dsDNA plasmid donor. PBac system was used to
287 facilitate genetic screening (Well Genetics). To generate ATP synthase OSCP-Apex2

288 under Marf-knockdown background, a stable line was selected by crossing ATP
289 synthase OSCP-Apex2 line with GAL4 (Bloomington 26882) line, which was
290 subsequently crossed with UAS (Bloomington 31157) line. To generate ATP synthase
291 OSCP-Apex2 under OPA1-knockdown background, a stable line was selected by
292 crossing ATP synthase OSCP-Apex2 line with GAL4 (Bloomington 38459) line,
293 which was subsequently crossed with UAS (Bloomington 32358) line.
294
295 ***HPF/FS specimen preparation for morphological observation***
296 Flies were anesthetized on ice and embedded in 4% low melting agarose in 0.1
297 M phosphate buffer. Embedded flies were then sectioned to 100 μm-thick slices by a
298 vibrating blade microtome (Leica VT1200S) and fixed in 2.5% glutaraldehyde in
299 phosphate buffer.
300 HPF/FS was also performed as previously described (Jiang, Lin et al., 2017a,
301 Jiang et al., 2017b). The tissue sections were washed in 3 drops (~150 μl) of
302 phosphate buffer, followed by 2 drops (~100 μl) of phosphate buffer with 20 % BSA.
303 The specimens were subsequently placed in the gold carrier filled with 20 % BSA in
304 PBS. The carriers were loaded into a high-pressure freezer (Leica EM HPM100)
305 according to manufacturer's instructions. The carriers were subsequently released
306 from the holder under liquid nitrogen and transferred to the chamber of a
307 freeze-substitution device (Leica EM AFS2) pre-cooled to -140 °C and incubated for
308 96 hr before FS.
309 During FS, the temperature of the chamber was raised to 0 °C at a slope of 5
310 °C/hr. During the process, the specimens were substituted with 0.1 % uranyl acetate
311 and 2 % glutaraldehyde in acetone at -60 °C for 12 hr, followed by 2 % osmium
312 tetroxide at -25 °C for 12 hr, and washed with acetone at 0 °C three times for 1 hr
313 each. The specimens were subsequently removed from the carriers using a needle,
314 infiltrated and embedded in EMBed-812 resin at room temperature, which was
315 polymerized at 65 °C for 16 hr. The specimen blocks were trimmed and sectioned
316 using an ultramicrotome. The sections were stained with Reynold's lead citrate for 10
317 min and subjected to TEM inspection.
318
319 ***Serial-section electron tomography***
320 The procedure was also performed as previously described (Jiang et al., 2017a,
321 Jiang et al., 2017b). Serial sections with a thickness of 200 nm were prepared and
322 collected on copper slot grids (2 x 0.5mm oval slots) with carbon supports, on which
323 overlaid with 10 nm fiducial gold pretreated with BSA. The grids were stained with
324 Reynold's lead citrate before the second layer of fiducial gold was applied. The
325 specimens were imaged with FEI Tecnai TEM operating at 200 kV and the
326 micrographs were recorded with a Gatan UltraScan 1000 CCD at 0.87 nm/pixel
327 (9,600x). Tilt series from -60˚ to +60˚ with 2˚ increments were acquired at 10 μm
328 defocus using Leginon automatic data collection software (Suloway, Shi et al., 2009).

329 Double tilt series were collected using a double tilt holder (Model 2040 Dual-Axis
330 Tomography Holder, Fischione). Serial tomograms were reconstructed, joined using
331 IMOD, and segmented using Avizo 3D software (FEI).
332

333 ***EM staining for COX activity***

334 The procedure was modified as previously described (Seligman, Karnovsky et al.,
335 1968). Vibrating blade microtome sections of the fly tissues were washed with PBS
336 and stained for 3 hr at 37 °C in a staining solution that contained 5 mg
337 3,3'-diaminobenzidine tetrahydrochloride (DAB), 9 ml sodium phosphate buffer
338 (0.05M, pH7.4), 750 mg sucrose, 20 μg catalase (dissolved in 0.05M potassium
339 phosphate buffer, pH 7.0), and 10 mg cytochrome c (dissolved in distilled water) at a
340 volume of 10 ml. Subsequently, the specimens were washed with PBS for 1 hr and
341 subjected to standard osmium fixation, dehydration, infiltration and embedded using
342 Embed-812 resin. The blocks were cut to thin-sections of 70 nm thicknesses and
343 observed under TEM without further staining.
344

345 ***HPF/FS specimen preparation for immuno-EM labeling***

346 Flies were sectioned in fixatives containing 4 % paraformaldehyde, 0.25 %
347 glutaraldehyde in phosphate buffer and subjected to HPF/FS as described above with
348 some modifications. Immuno-EM specimens were freeze-substituted with 0.1 %
349 uranyl acetate in acetone at -90 °C for 58 hr (agitated every 8 hr), and warmed up to
350 -45 °C at a slope of 5 °C /hr, washed with acetone three times for 1 hr each. The
351 specimens were subsequently infiltrated through an ascending gradient of Lowicryl
352 HM20 resin (10%, 20%, 40%, 60%, 80% and 90%, 8hr for each concentration, and
353 agitated every 2 hr). The chamber was further warmed up to -25 °C at 5 °C /hr. The
354 solutions were replaced with 100 % HM20 three times for 24 hr each (agitated every
355 2 hr). After adjusting the orientation within the carriers, ultraviolet polymerization
356 was performed at -25 °C for 48 hr. The chamber was later warmed up to 20 °C (5°C
357 /hr) and exposed to ultraviolet radiation for another 48 hr.
358 After polymerization, the specimen blocks were detached from HPF carriers. 100
359 nm thick sections were prepared and placed on 200-mesh nickel grids for
360 immuno-EM labeling.
361

362 ***Immuno-EM labeling***

363 Thin sections placed on nickel grids were blocked with 10 % BSA in PBS for 20
364 min and incubated with primary antibodies in incubation buffer (1% BSA in PBS) for
365 2 hr. Grids were subsequently washed with incubation buffer three times (10 min
366 each). Secondary antibodies, goat anti-mouse IgG (EM.GMHL15, BB International)
367 and protein A (EM.PAG15, BB International) conjugated to 15 nm gold particles,
368 were used against the primary antibodies from mouse and rabbit respectively.

369 Secondary antibodies at 20-fold dilution were applied and samples were incubated for
370 1 hr. After washing with PBS, the immune-complexes were fixed with 1%
371 glutaraldehyde in PBS and washed three times with distilled water. The specimens
372 were inspected by TEM operating at 120 kV (FEI Tecnai G2 TF20 Super TWIN).
373 The primary antibodies and applied dilution factors are listed as follows: mouse
374 anti-dsDNA (500x, abcam ab27156), mouse anti-ATP5A (500x, abcam ab14748),
375 mouse anti-Cytochrome C (8000x, abcam ab13575), mouse anti-PDHA1 (500x,
376 abcam ab110334), mouse anti-Ubiquitin (1000x, abcam ab7254), mouse
377 anti-DNA-RNA hybrid (500x, kerafast ENH001), and rabbit anti-SOD2 (500x, abcam
378 ab13534).
379
380 ***Apex2 staining EM***
381 The protocol was modified as previously described (Hung, Udeshi et al., 2016).
382 Vibratome sections of the fly tissues were fixed in 2% glutaraldehyde in 0.1 M
383 sodium cacodylate with 2 mM $CaCl_2$, pH 7. Residual glutaraldehyde was quenched
384 with 20 mM glycine followed by the washing steps. The specimens were
385 subsequently stained with 0.5 mg/ml DAB-4HCL (3,3′-diaminobenzidine) and 0.3%
386 H_2O_2 in the buffer for 30 min, washed, and stained with 1% osmium tetroxide for 30
387 min. After washes, the specimens were stained with 1% uranyl acetate overnight. The
388 specimens were further dehydrated and embedded in resin for thin-section and TEM
389 observation.
390
391 ***Cell culture for Apex2 staining***
392 293T cells were seeded on plastic membranes in a 6-well culture plate. The cells
393 reached >80% confluence after overnight culture and were transfected with
394 pECFP-OPA1 (human isoform1)-Apex2-Flag using *Trans*IT-X2 (Thermo-Fisher).
395 After incubation overnight, the monolayer cells were fixed with 2% glutaraldehyde
396 and followed the Apex2 staining procedure as described above (Hung et al., 2016).
397 S2 cells were seeded in a 6-well culture plate at $1*10^6$ cells/ml and grew for
398 another day to $2\text{-}4*10^6$ cells/ml. The cells were transfected with
399 pMT-V5-HisB-OXA1 (*D. melanogaster*)-Apex2-Flag or pMT-V5-HisB-OPA1 (*D.*
400 *melanogaster*)-Apex2-Flag using calcium phosphate transfection kit (Invitrogen) and
401 induced protein expression by $CuSO_4$. The cells were harvested 2-3 days
402 post-induction, fixed with 2% glutaraldehyde and followed the Apex2 staining
403 procedure as described above (Hung et al., 2016).
404
405 ***Western blot analysis***
406 Flies were dissected and homogenized by Dounce tissue grinder in RIPA
407 buffer containing protease inhibitor (cOmplete™, Roche). Cellular debris was
408 removed by centrifugation at 4℃, 14000 x g for 20 min. The supernatants were
409 collected and the protein concentrations were determined by Pierce protein

assay (Pierce 660 nm Protein Assay Reagent, ThermoScientific). 0.6 μg/well of proteins were loaded for SDS-PAGE and western-blot analysis.

The antibodies used in the studies were as follows: mouse anti-ATP5A (50000x, abcam ab14748), mouse anti-Cytochrome C (10000x, abcam ab13575), mouse anti-PDHA1 (1000x, abcam ab110334) or rabbit anti-SOD2 (10000x, abcam ab13534), and rabbit anti-alpha tubulin (10000x, abcam ab18251), anti-mouse IgG-HRP (2000x, Invitrogen 62-6520) or anti-rabbit IgG-HRP (5000x, abcam ab97051). For quantification, ratios of the densitometry signal of individual proteins to that of alpha-tubulin were calculated. The ratios were then normalized to the wild type at week 4.

Mitochondria analysis

The changes in the mitochondrial size of Marf and OPA1-knockdown vs. the wild type were calculated using thin-section EM micrographs. For each type, over a hundred mitochondria were analyzed. The cristae to mitochondrial membrane content of Marf-knockdown vs. the wild type were analyzed using semi-automatic segmentation function of Avizo 3D.

Climbing assay

Flies were knocked down to the bottom of the culture tubes. Numbers of flies climbing over the target line (about 18cm) over 3 min were recorded. About 15 flies were used for each triplicate.

Acknowledgments

We thank the EM core of Institute of Cellular and Organismic Biology and the cryo-EM core of Academia Sinica, Taiwan. We thank Dr. Ya-Hui Chou for the helpful discussion on *Drosophila* genetics. We thank the funding support from Academia Sinica AS-105-TP-B04 and MOST 105-2628-B-001-004-MY3.

Author contributions

Yi-fan Jiang and Chi-yu Fu designed the experiments; Yi-fan Jiang, Hsiang-ling Lin, Li-jie Wang, and Tian Hsu performed the experiments; Chi-yu Fu wrote the paper.

Competing interests: The authors declare no competing financial interests.

References

Agrell I (1953) The aerobic and anaerobic utilization of metabolic energy during insect metamorphosis. Acta Physiol Scand 28: 306-35

450 Area-Gomez E, Del Carmen Lara Castillo M, Tambini MD, Guardia-Laguarta C, de
451 Groof AJ, Madra M, Ikenouchi J, Umeda M, Bird TD, Sturley SL, Schon EA (2012)
452 Upregulated function of mitochondria-associated ER membranes in Alzheimer
453 disease. EMBO J 31: 4106-23
454 Ban T, Ishihara T, Kohno H, Saita S, Ichimura A, Maenaka K, Oka T, Mihara K,
455 Ishihara N (2017) Molecular basis of selective mitochondrial fusion by
456 heterotypic action between OPA1 and cardiolipin. Nat Cell Biol 19: 856-863
457 Bonifacino JS, Glick BS (2004) The mechanisms of vesicle budding and fusion.
458 Cell 116: 153-66
459 Cogliati S, Enriquez JA, Scorrano L (2016) Mitochondrial Cristae: Where Beauty
460 Meets Functionality. Trends Biochem Sci 41: 261-273
461 Cogliati S, Frezza C, Soriano ME, Varanita T, Quintana-Cabrera R, Corrado M,
462 Cipolat S, Costa V, Casarin A, Gomes LC, Perales-Clemente E, Salviati L,
463 Fernandez-Silva P, Enriquez JA, Scorrano L (2013) Mitochondrial cristae shape
464 determines respiratory chain supercomplexes assembly and respiratory
465 efficiency. Cell 155: 160-71
466 Davies KM, Strauss M, Daum B, Kief JH, Osiewacz HD, Rycovska A, Zickermann V,
467 Kuhlbrandt W (2011) Macromolecular organization of ATP synthase and
468 complex I in whole mitochondria. Proceedings of the National Academy of
469 Sciences of the United States of America 108: 14121-6
470 de Brito OM, Scorrano L (2008) Mitofusin 2 tethers endoplasmic reticulum to
471 mitochondria. Nature 456: 605-10
472 Del Dotto V, Mishra P, Vidoni S, Fogazza M, Maresca A, Caporali L, McCaffery JM,
473 Cappelletti M, Baruffini E, Lenaers G, Chan D, Rugolo M, Carelli V, Zanna C (2017)
474 OPA1 Isoforms in the Hierarchical Organization of Mitochondrial Functions. Cell
475 Rep 19: 2557-2571
476 Desmurs M, Foti M, Raemy E, Vaz FM, Martinou JC, Bairoch A, Lane L (2015)
477 C11orf83, a mitochondrial cardiolipin-binding protein involved in bc1 complex
478 assembly and supercomplex stabilization. Mol Cell Biol 35: 1139-56
479 Detmer SA, Chan DC (2007) Functions and dysfunctions of mitochondrial
480 dynamics. Nat Rev Mol Cell Biol 8: 870-9
481 Elachouri G, Vidoni S, Zanna C, Pattyn A, Boukhaddaoui H, Gaget K, Yu-Wai-Man P,
482 Gasparre G, Sarzi E, Delettre C, Olichon A, Loiseau D, Reynier P, Chinnery PF,
483 Rotig A, Carelli V, Hamel CP, Rugolo M, Lenaers G (2011) OPA1 links human
484 mitochondrial genome maintenance to mtDNA replication and distribution.
485 Genome Res 21: 12-20
486 Filadi R, Greotti E, Turacchio G, Luini A, Pozzan T, Pizzo P (2015) Mitofusin 2
487 ablation increases endoplasmic reticulum-mitochondria coupling. Proc Natl Acad
488 Sci U S A 112: E2174-81
489 Filadi R, Pendin D, Pizzo P (2018) Mitofusin 2: from functions to disease. Cell
490 Death Dis 9: 330

491 Flis VV, Daum G (2013) Lipid transport between the endoplasmic reticulum and
492 mitochondria. Cold Spring Harb Perspect Biol 5
493 Frezza C, Cipolat S, Martins de Brito O, Micaroni M, Beznoussenko GV, Rudka T,
494 Bartoli D, Polishuck RS, Danial NN, De Strooper B, Scorrano L (2006) OPA1
495 controls apoptotic cristae remodeling independently from mitochondrial fusion.
496 Cell 126: 177-89
497 Gilkerson RW, Selker JM, Capaldi RA (2003) The cristal membrane of
498 mitochondria is the principal site of oxidative phosphorylation. FEBS Lett 546:
499 355-8
500 Gold VA, Chroscicki P, Bragoszewski P, Chacinska A (2017) Visualization of
501 cytosolic ribosomes on the surface of mitochondria by electron cryo-tomography.
502 EMBO Rep 18: 1786-1800
503 Harbauer AB, Zahedi RP, Sickmann A, Pfanner N, Meisinger C (2014) The protein
504 import machinery of mitochondria-a regulatory hub in metabolism, stress, and
505 disease. Cell Metab 19: 357-72
506 Harner ME, Unger AK, Geerts WJ, Mari M, Izawa T, Stenger M, Geimer S, Reggiori
507 F, Westermann B, Neupert W (2016) An evidence based hypothesis on the
508 existence of two pathways of mitochondrial crista formation. Elife 5
509 Hoppins S, Collins SR, Cassidy-Stone A, Hummel E, Devay RM, Lackner LL,
510 Westermann B, Schuldiner M, Weissman JS, Nunnari J (2011) A
511 mitochondrial-focused genetic interaction map reveals a scaffold-like complex
512 required for inner membrane organization in mitochondria. The Journal of cell
513 biology 195: 323-40
514 Hung V, Udeshi ND, Lam SS, Loh KH, Cox KJ, Pedram K, Carr SA, Ting AY (2016)
515 Spatially resolved proteomic mapping in living cells with the engineered
516 peroxidase APEX2. Nat Protoc 11: 456-75
517 Huynen MA, Muhlmeister M, Gotthardt K, Guerrero-Castillo S, Brandt U (2016)
518 Evolution and structural organization of the mitochondrial contact site (MICOS)
519 complex and the mitochondrial intermembrane space bridging (MIB) complex.
520 Biochimica et biophysica acta 1863: 91-101
521 Jayashankar V, Mueller IA, Rafelski SM (2016) Shaping the multi-scale
522 architecture of mitochondria. Current opinion in cell biology 38: 45-51
523 Jiang YF, Lin HL, Fu CY (2017a) 3D Mitochondrial Ultrastructure of Drosophila
524 Indirect Flight Muscle Revealed by Serial-section Electron Tomography. Journal
525 of visualized experiments : JoVE
526 Jiang YF, Lin SS, Chen JM, Tsai HZ, Hsieh TS, Fu CY (2017b) Electron tomographic
527 analysis reveals ultrastructural features of mitochondrial cristae architecture
528 which reflect energetic state and aging. Sci Rep 7: 45474
529 Keil M, Bareth B, Woellhaf MW, Peleh V, Prestele M, Rehling P, Herrmann JM
530 (2012) Oxa1-ribosome complexes coordinate the assembly of cytochrome C
531 oxidase in mitochondria. The Journal of biological chemistry 287: 34484-93

532 Khalil B, Cabirol-Pol MJ, Miguel L, Whitworth AJ, Lecourtois M, Lievens JC (2017)
533 Enhancing Mitofusin/Marf ameliorates neuromuscular dysfunction in Drosophila
534 models of TDP-43 proteinopathies. Neurobiol Aging 54: 71-83
535 MacVicar T, Langer T (2016) OPA1 processing in cell death and disease - the long
536 and short of it. J Cell Sci 129: 2297-306
537 Mannella CA (2006) Structure and dynamics of the mitochondrial inner
538 membrane cristae. Biochimica et biophysica acta 1763: 542-8
539 Martell JD, Deerinck TJ, Sancak Y, Poulos TL, Mootha VK, Sosinsky GE, Ellisman
540 MH, Ting AY (2012) Engineered ascorbate peroxidase as a genetically encoded
541 reporter for electron microscopy. Nature biotechnology 30: 1143-8
542 Paradies G, Paradies V, De Benedictis V, Ruggiero FM, Petrosillo G (2014)
543 Functional role of cardiolipin in mitochondrial bioenergetics. Biochimica et
544 biophysica acta 1837: 408-17
545 Picard M, McManus MJ, Csordas G, Varnai P, Dorn GW, 2nd, Williams D,
546 Hajnoczky G, Wallace DC (2015) Trans-mitochondrial coordination of cristae at
547 regulated membrane junctions. Nat Commun 6: 6259
548 Quintana-Cabrera R, Quirin C, Glytsou C, Corrado M, Urbani A, Pellattiero A, Calvo
549 E, Vazquez J, Enriquez JA, Gerle C, Soriano ME, Bernardi P, Scorrano L (2018) The
550 cristae modulator Optic atrophy 1 requires mitochondrial ATP synthase
551 oligomers to safeguard mitochondrial function. Nat Commun 9: 3399
552 Rampelt H, Zerbes RM, van der Laan M, Pfanner N (2017) Role of the
553 mitochondrial contact site and cristae organizing system in membrane
554 architecture and dynamics. Biochimica et biophysica acta 1864: 737-746
555 Sandoval H, Yao CK, Chen K, Jaiswal M, Donti T, Lin YQ, Bayat V, Xiong B, Zhang K,
556 David G, Charng WL, Yamamoto S, Duraine L, Graham BH, Bellen HJ (2014)
557 Mitochondrial fusion but not fission regulates larval growth and synaptic
558 development through steroid hormone production. Elife 3
559 Sastri M, Darshi M, Mackey M, Ramachandra R, Ju S, Phan S, Adams S, Stein K,
560 Douglas CR, Kim JJ, Ellisman MH, Taylor SS, Perkins GA (2017)
561 Sub-mitochondrial localization of the genetic-tagged mitochondrial
562 intermembrane space-bridging components Mic19, Mic60 and Sam50. J Cell Sci
563 130: 3248-3260
564 Schorr S, van der Laan M (2017) Integrative functions of the mitochondrial
565 contact site and cristae organizing system. Semin Cell Dev Biol
566 Schrepfer E, Scorrano L (2016) Mitofusins, from Mitochondria to Metabolism.
567 Molecular cell 61: 683-694
568 Scorrano L, Ashiya M, Buttle K, Weiler S, Oakes SA, Mannella CA, Korsmeyer SJ
569 (2002) A distinct pathway remodels mitochondrial cristae and mobilizes
570 cytochrome c during apoptosis. Dev Cell 2: 55-67
571 Seligman AM, Karnovsky MJ, Wasserkrug HL, Hanker JS (1968) Nondroplet
572 ultrastructural demonstration of cytochrome oxidase activity with a

573 polymerizing osmiophilic reagent, diaminobenzidine (DAB). J Cell Biol 38: 1-14
574 Song Z, Chen H, Fiket M, Alexander C, Chan DC (2007) OPA1 processing controls
575 mitochondrial fusion and is regulated by mRNA splicing, membrane potential,
576 and Yme1L. The Journal of cell biology 178: 749-55
577 Soto IC, Fontanesi F, Liu J, Barrientos A (2012) Biogenesis and assembly of
578 eukaryotic cytochrome c oxidase catalytic core. Biochimica et biophysica acta
579 1817: 883-97
580 Stoldt S, Wenzel D, Hildenbeutel M, Wurm CA, Herrmann JM, Jakobs S (2012) The
581 inner-mitochondrial distribution of Oxa1 depends on the growth conditions and
582 on the availability of substrates. Mol Biol Cell 23: 2292-301
583 Strauss M, Hofhaus G, Schroder RR, Kuhlbrandt W (2008) Dimer ribbons of ATP
584 synthase shape the inner mitochondrial membrane. EMBO J 27: 1154-60
585 Suloway C, Shi J, Cheng A, Pulokas J, Carragher B, Potter CS, Zheng SQ, Agard DA,
586 Jensen GJ (2009) Fully automated, sequential tilt-series acquisition with Leginon.
587 Journal of structural biology 167: 11-8
588 Tatsuta T, Langer T (2017) Intramitochondrial phospholipid trafficking. Biochim
589 Biophys Acta 1862: 81-89
590 Tennessen JM, Baker KD, Lam G, Evans J, Thummel CS (2011) The Drosophila
591 estrogen-related receptor directs a metabolic switch that supports
592 developmental growth. Cell metabolism 13: 139-48
593 Vance JE (2014) MAM (mitochondria-associated membranes) in mammalian
594 cells: lipids and beyond. Biochim Biophys Acta 1841: 595-609
595 Varanita T, Soriano ME, Romanello V, Zaglia T, Quintana-Cabrera R, Semenzato M,
596 Menabo R, Costa V, Civiletto G, Pesce P, Viscomi C, Zeviani M, Di Lisa F, Mongillo
597 M, Sandri M, Scorrano L (2015) The OPA1-dependent mitochondrial cristae
598 remodeling pathway controls atrophic, apoptotic, and ischemic tissue damage.
599 Cell metabolism 21: 834-44
600 Wu M, Gu J, Guo R, Huang Y, Yang M (2016) Structure of Mammalian Respiratory
601 Supercomplex I1III2IV1. Cell 167: 1598-1609 e10
602 Zhou A, Rohou A, Schep DG, Bason JV, Montgomery MG, Walker JE, Grigorieff N,
603 Rubinstein JL (2015) Structure and conformational states of the bovine
604 mitochondrial ATP synthase by cryo-EM. Elife 4: e10180

605 **Figure legends**

606 **Fig 1. 3D visualization of mitochondrial development upon *Drosophila* eclosion.**
607 A thin-section TEM micrograph of *Drosophila* IFM at day 1 (a) and week 4 (b). A
608 slice of a serial-section tomography reconstruction (c) and the segmentation (d) of
609 *Drosophila* IFM at day 1. (a) red arrows: cytoplasmic ribosomal-like densities; (d)
610 blue: cristae; red: mitochondrial ribosomal-like densities; green: cytoplasmic
611 ribosomal-like densities.
612

613 **Fig 2. Analysis of protein contents during mitochondrial development.**
614 Immuno-EM labeling of ATP5A of *Drosophila* IFM at day 1 (a) and week 4 (b).
615 Western-blot analysis of mitochondrial proteins ATP5A, PDHA1, SOD2, CytC and
616 ribosomal protein RPS6 of *Drosophila* at day 1, week 1, and week 4 (c). The relative
617 protein abundance was quantified by densitometry and normalized to the signal of
618 α-tubulin. The ratios were subsequently normalized to those of weak4.
619
620 **Fig 3. Cristae morphogenesis coordinates with COX assembly**
621 A thin-section TEM micrograph of *Drosophila* IFM at day 1 (a) and week 4 (b)
622 stained for COX activity. Tomographic slices across the z-axis and the corresponding
623 segmentation of *Drosophila* IFM at day 1 stained for COX activity were shown (c).
624 3D representations of the tomographic segmentation were shown in (d) and (e). (c-e),
625 red: COX-positive cristae; yellow: COX-negative reticular membranes. Positive COX
626 activity appeared darkly stained in the micrographs.
627
628 **Fig 4. Ultrastructural tracking of COX4 and OXA1 during cristae biogenesis**
629 Apex2 staining of the IFM of COX4-Apex2 knockin flies (a) and OXA1-Apex2
630 knockin flies (c) at day 1 were shown. Apex2 staining of the wild type at day 1 as
631 negative controls were shown in (b) and (d), respectively. Apex2 staining of S2 cells
632 transfected with and without plasmids expressing *D. melanogaster* OXA1-Apex2 was
633 shown in (e) and (f), respectively. Positive Apex2 signals appeared darkly stained in
634 the micrographs.
635
636 **Fig 5. Marf-knockdown flies formed lamellar cristae containing COX and ATP**
637 **synthase**
638 Thin-section TEM micrograph (a), the tomographic segmentation (b-d), COX activity
639 staining (e), immuno-EM against ATP5A (f), and ATP synthase OSCP-Apex2
640 staining (g) of Marf-knockdown flies at week 4 were shown. Positive Apex2 signal or
641 COX activity appeared darkly stained in the micrographs.
642
643 **Fig 6. OPA1-knockdown flies showed impaired cristae biogenesis**
644 OPA1-knockdown flies at day 1 were analyzed by thin-section TEM (a), COX
645 activity staining (b), immuno-EM against ATP5A (c), ATP synthase OSCP-Apex2
646 staining (d), and the tomographic segmentation (f). Sub-mitochondrial localization of
647 OPA1 was tracked in 293T cells overexpressing human OPA1-Apex2 (e).

Fig 1

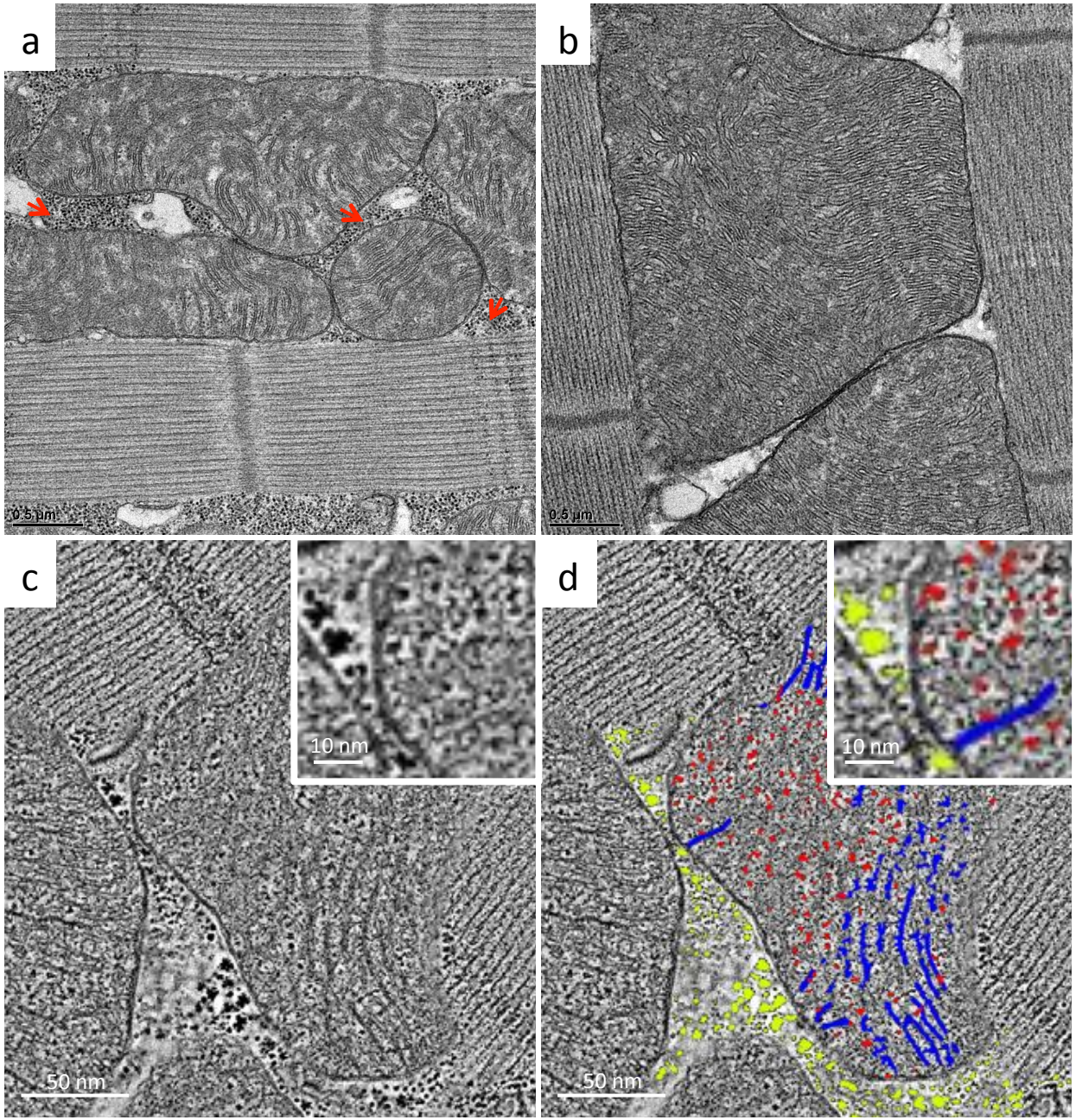

Fig 2

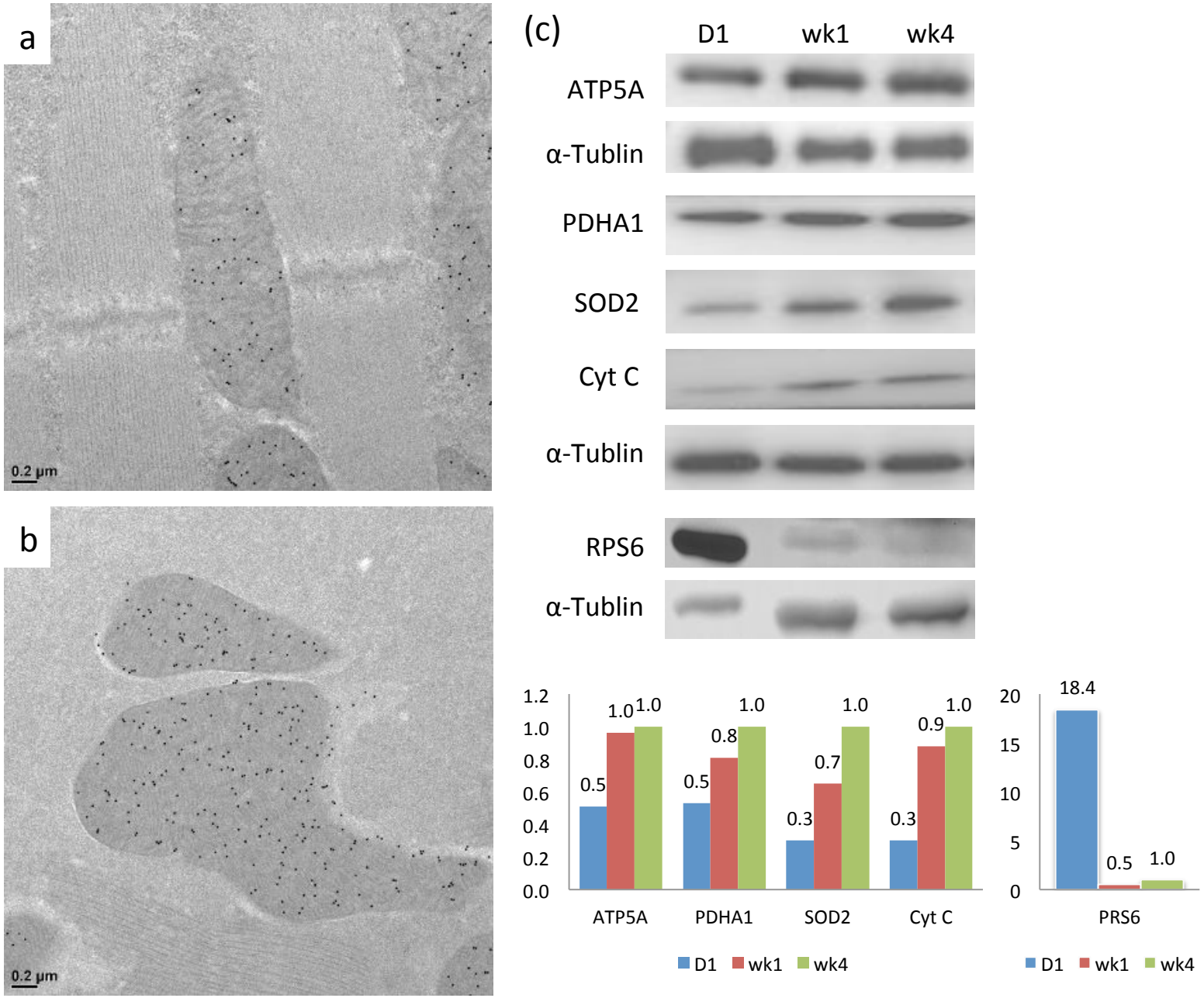
a
0.2 μm
b
0.2 μm
(c)
D1
wk1
wk4
ATP5A
α-Tublin
PDHA1
SOD2
Cyt C
α-Tublin
RPS6
α-Tublin
1.2
1.0
0.8
0.6
0.4
0.2
0.0
0.5
1.0
1.0
0.5
0.8
1.0
0.3
0.7
1.0
0.3
0.9
1.0
ATP5A
PDHA1
SOD2
Cyt C
D1
wk1
wk4
20
15
10
5
0
18.4
0.5
1.0
PRS6
D1
wk1
wk4

Fig 3

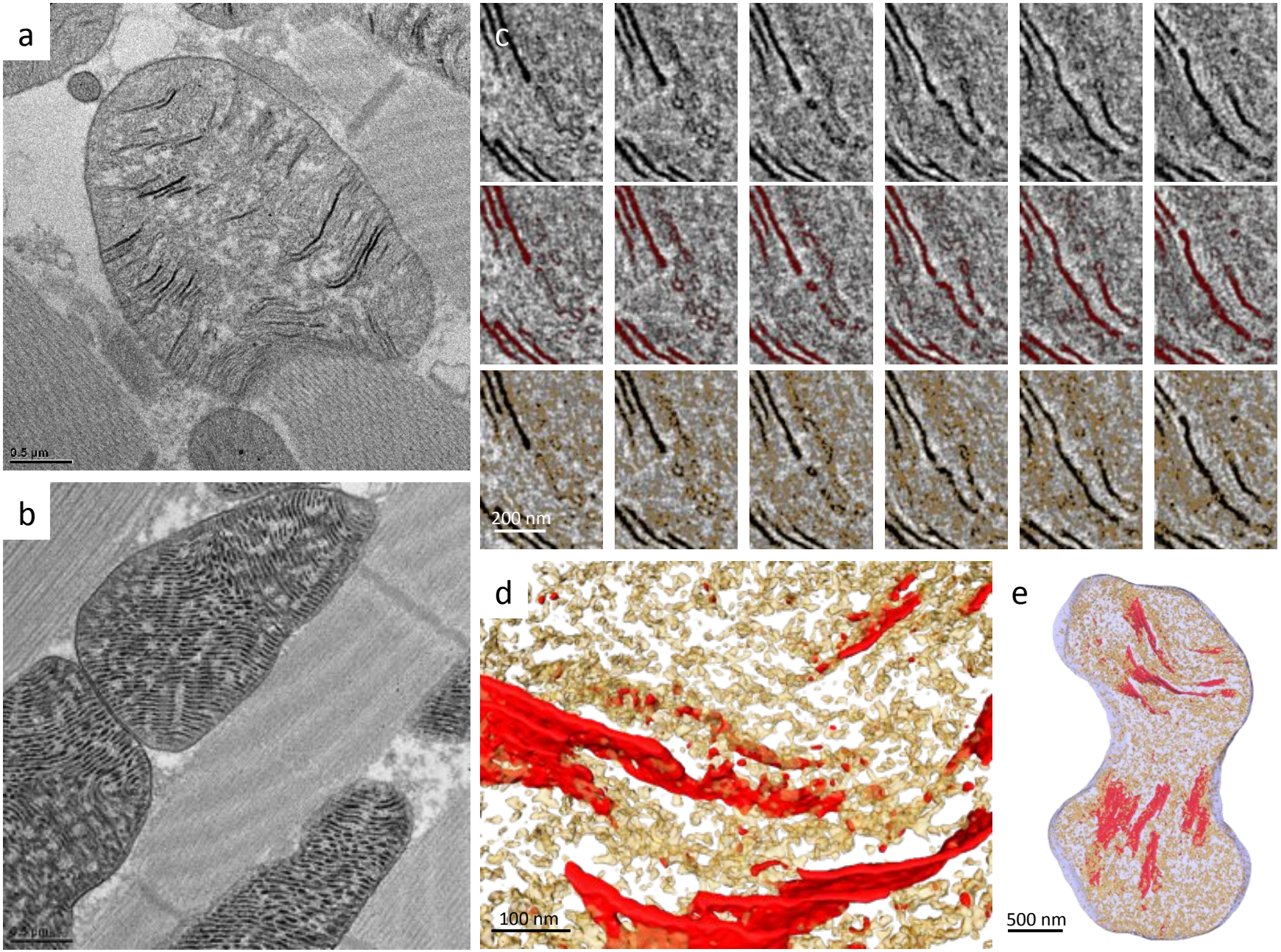

Fig 4

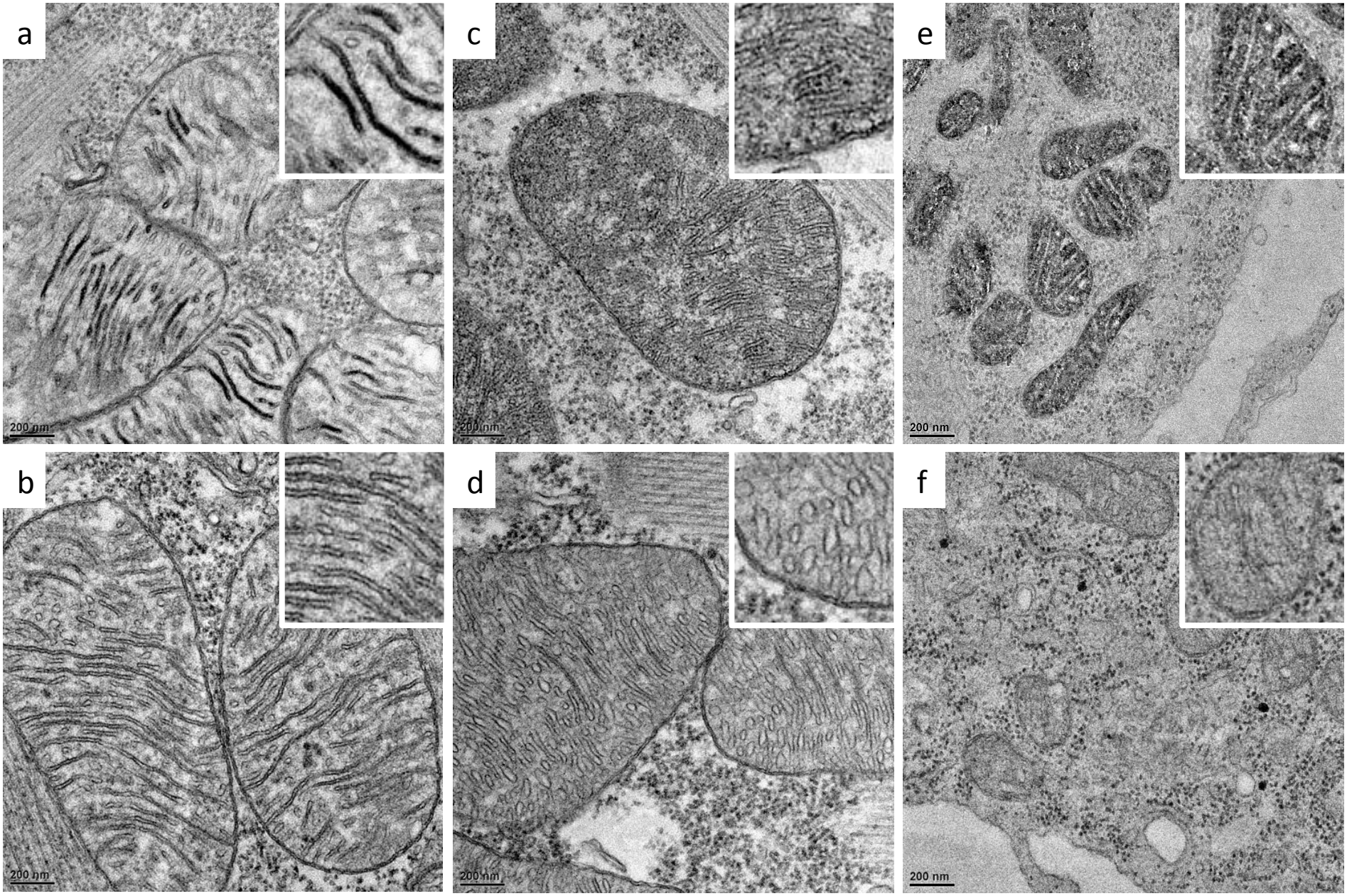

Fig 5

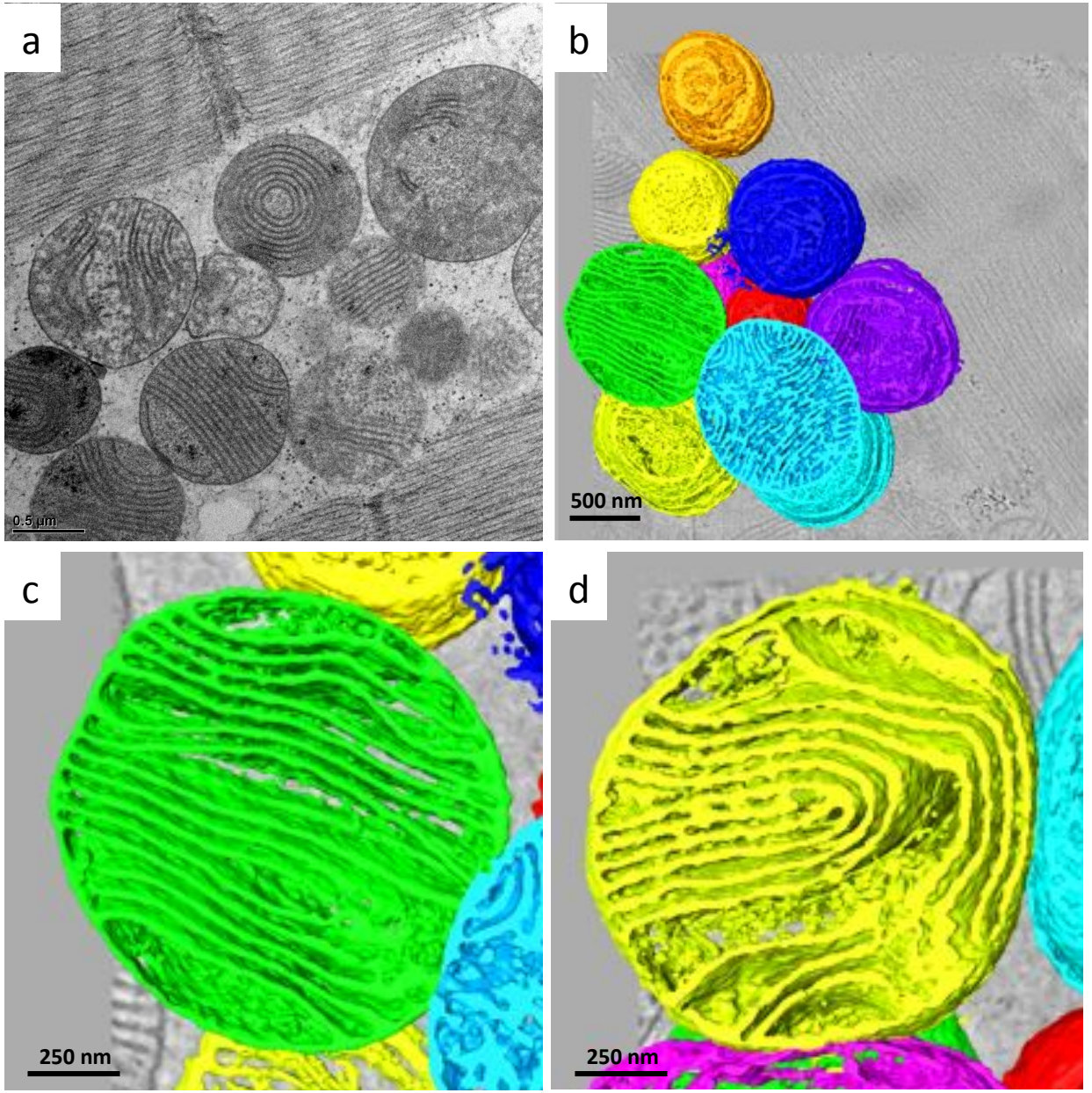

Fig 5

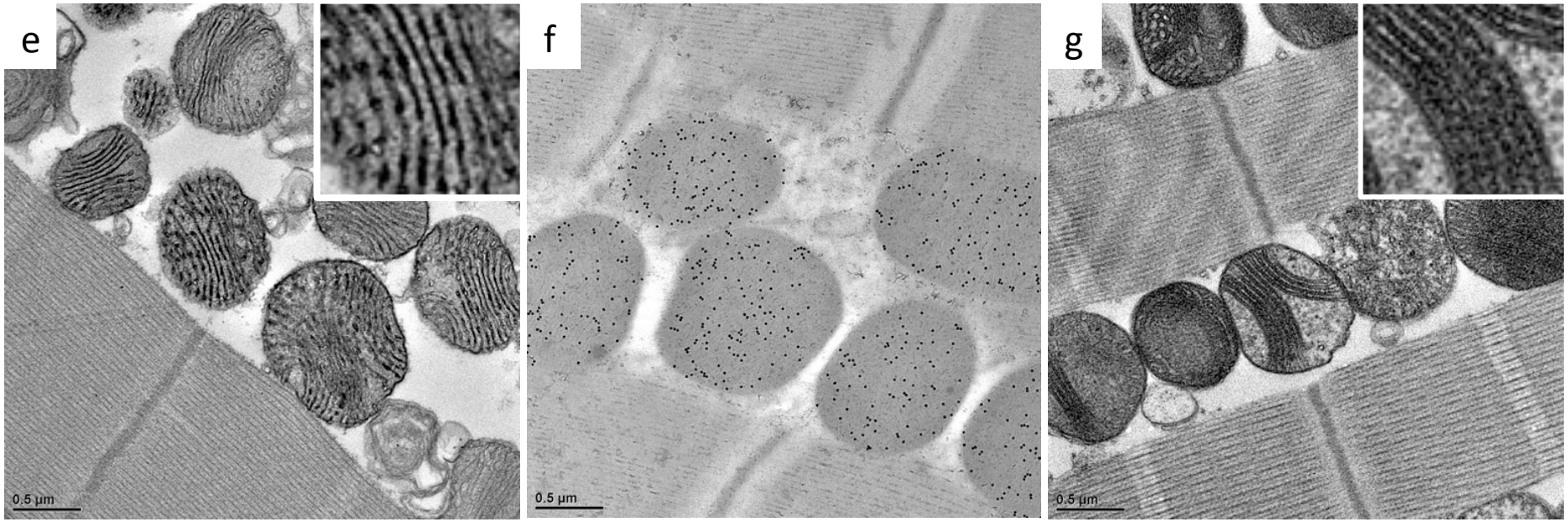

Fig 6

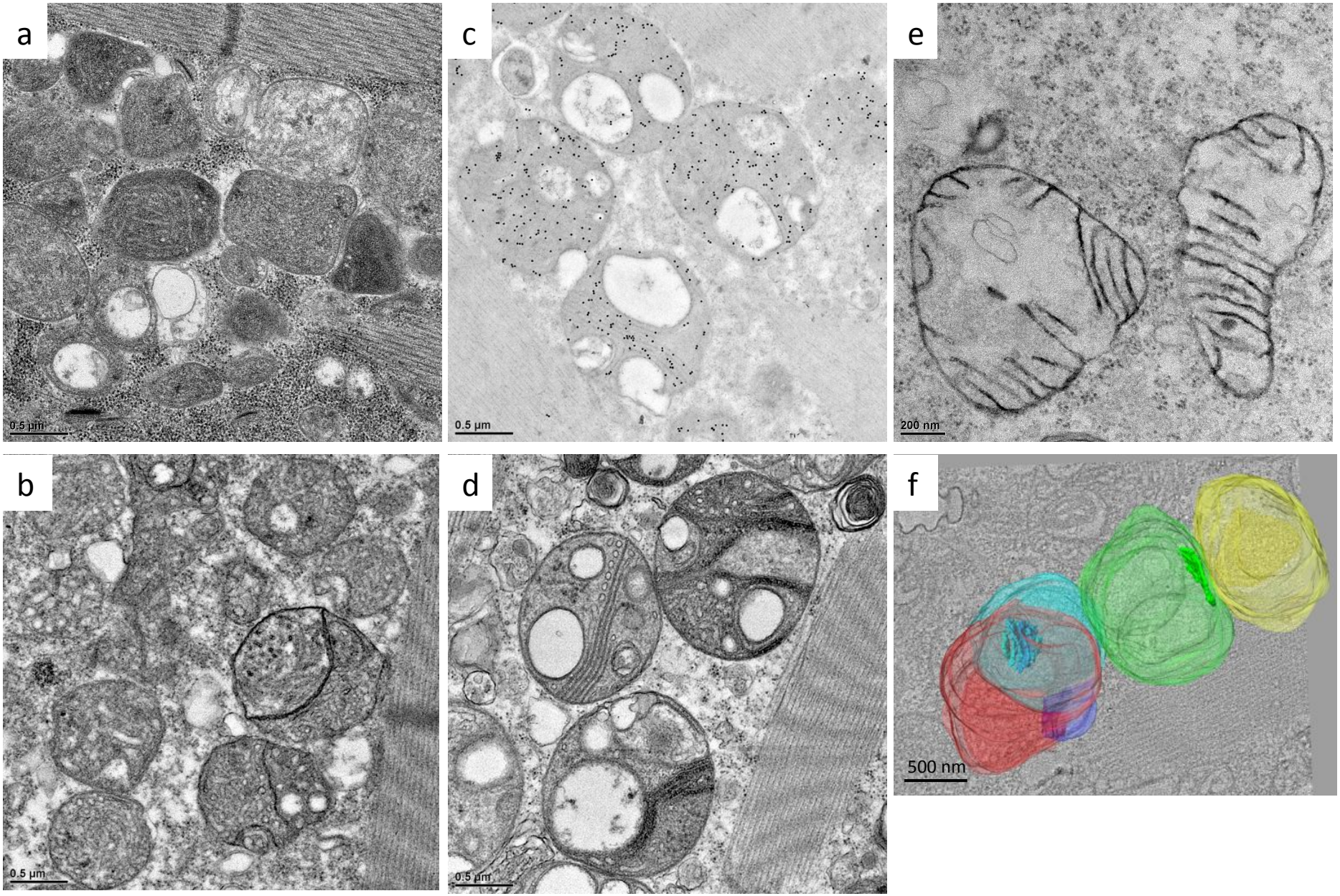

Fig S1

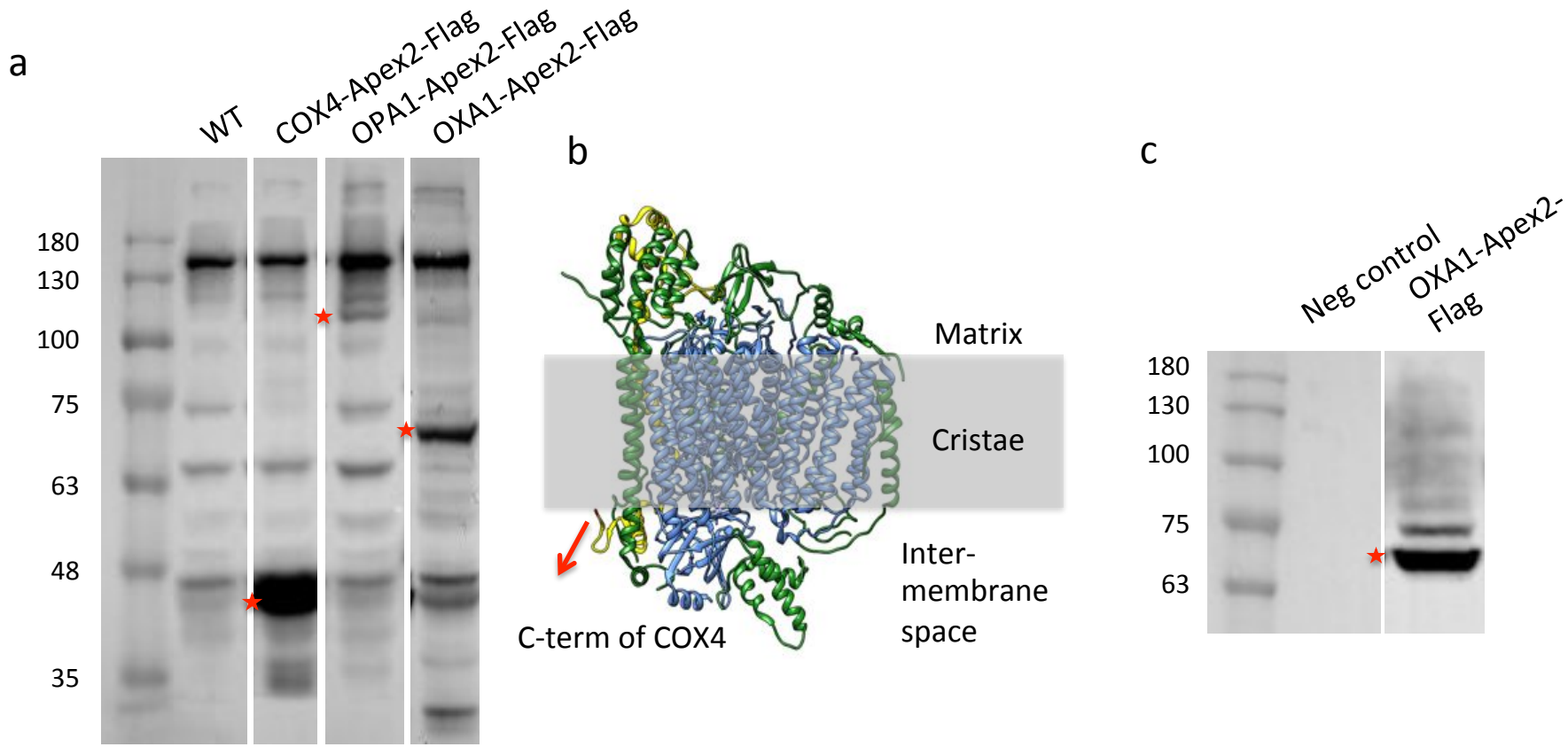
a
WT
COX4-Apex2-Flag
OPA1-Apex2-Flag
OXA1-Apex2-Flag
180
130
100
75
63
48
35
b
Matrix
Cristae
Inter-
membrane
space
C-term of COX4
c
Neg control
OXA1-Apex2-
Flag
180
130
100
75
63

Fig S2

(a)

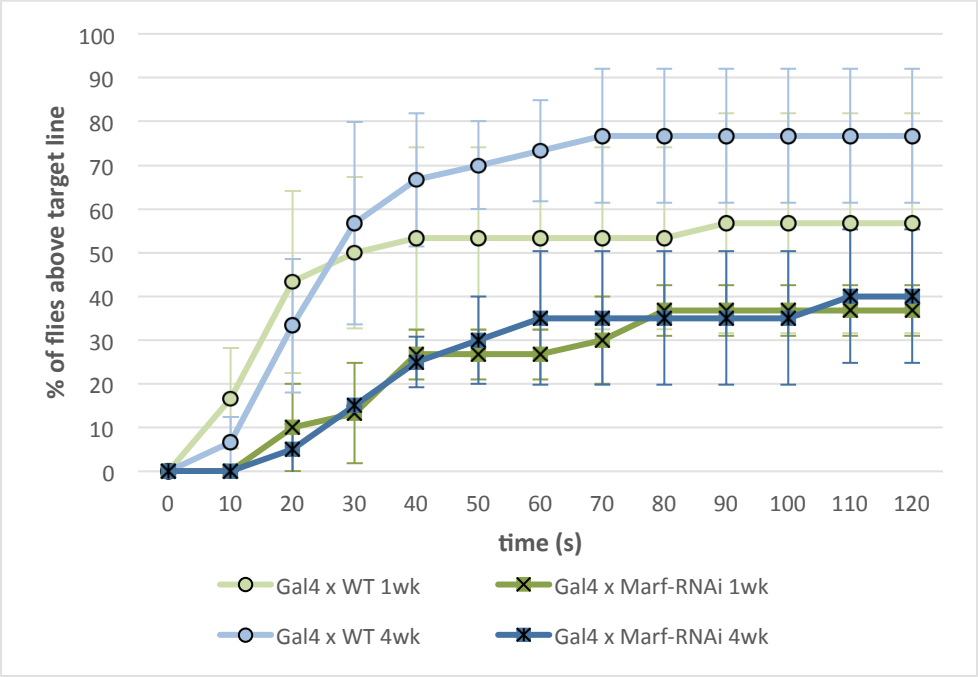
100
90
80
70
60
50
40
30
20
10
0
% of flies above target line
0
10
20
30
40
50
60
70
80
90
100
110
120
time (s)
Gal4 x WT 1wk
Gal4 x Marf-RNAi 1wk
Gal4 x WT 4wk
Gal4 x Marf-RNAi 4wk

(b)

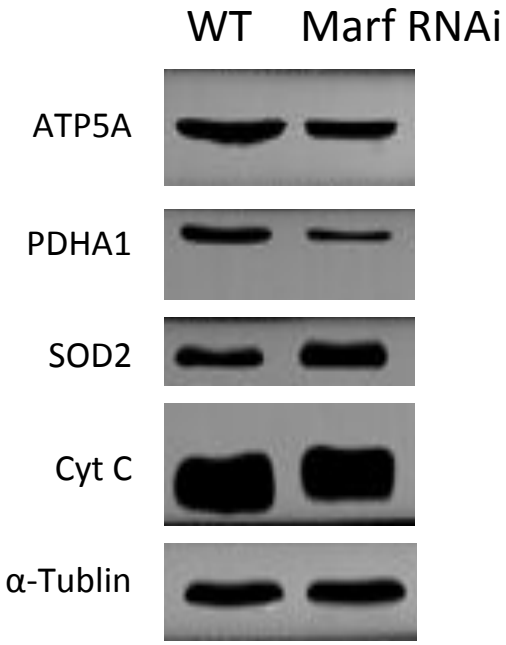
WT
Marf RNAi
ATP5A
PDHA1
SOD2
Cyt C
α-Tublin

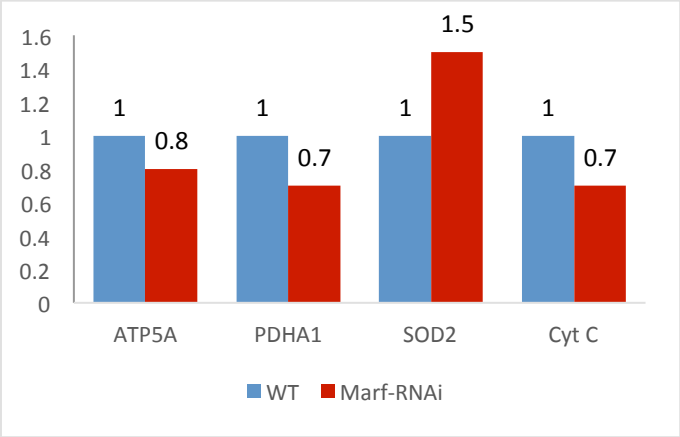
1.6
1.4
1.2
1
0.8
0.6
0.4
0.2
0
1
0.8
1
0.7
1
1.5
1
0.7
ATP5A
PDHA1
SOD2
Cyt C
WT
Marf-RNAi

Fig S2

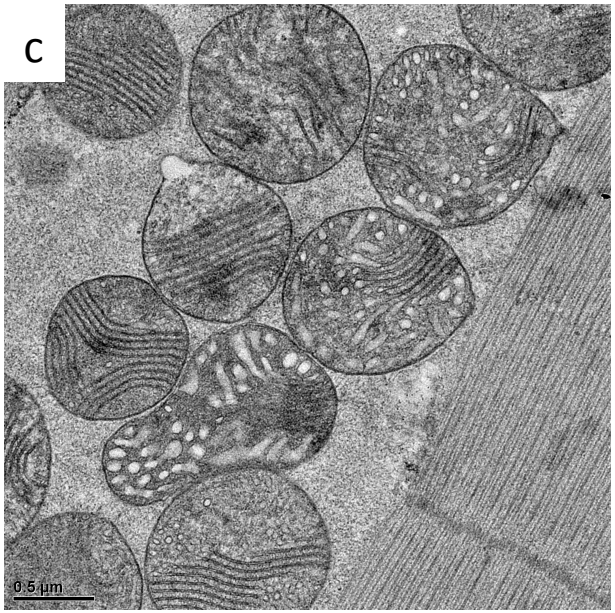
c
0.5 µm

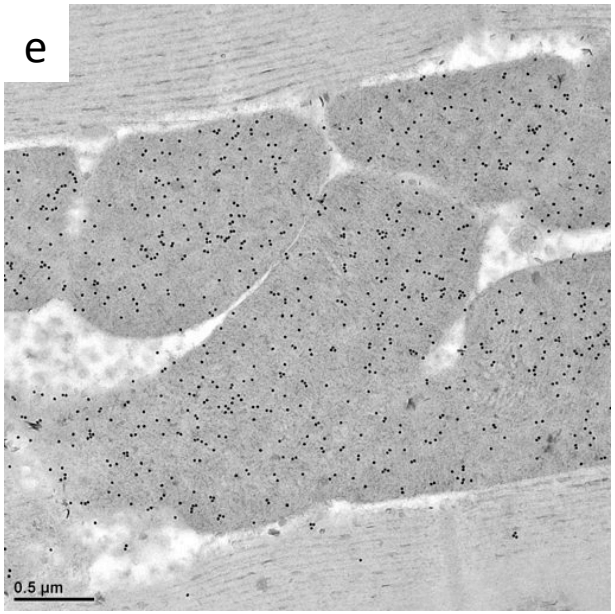
e
0.5 µm

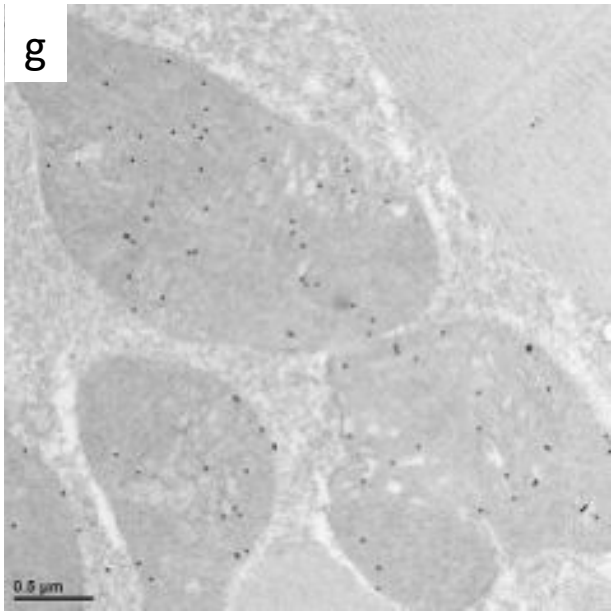
g
0.5 µm

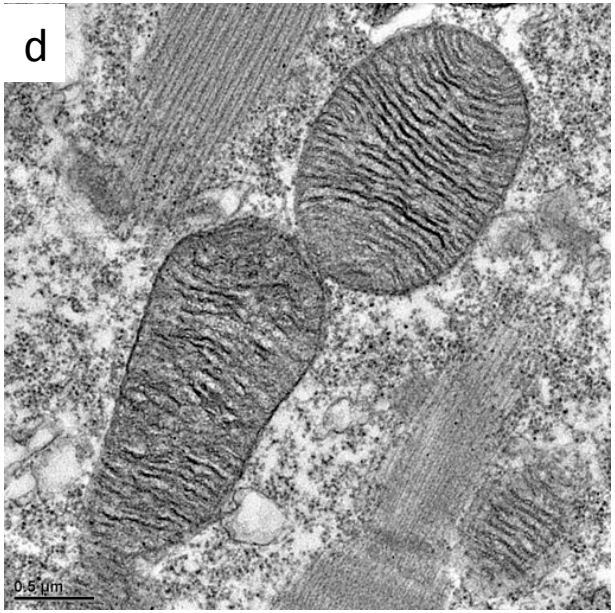
d
0.5 µm

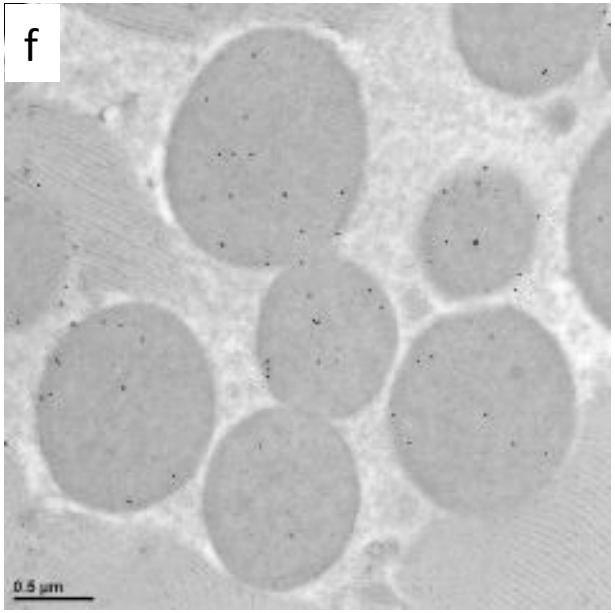
f
0.5 µm

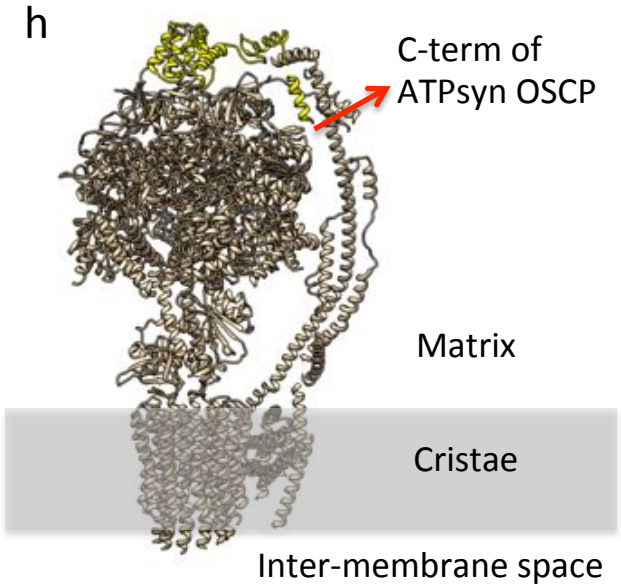
h
C-term of
ATPsyn OSCP
Matrix
Cristae
Inter-membrane space

Fig S3

(a)

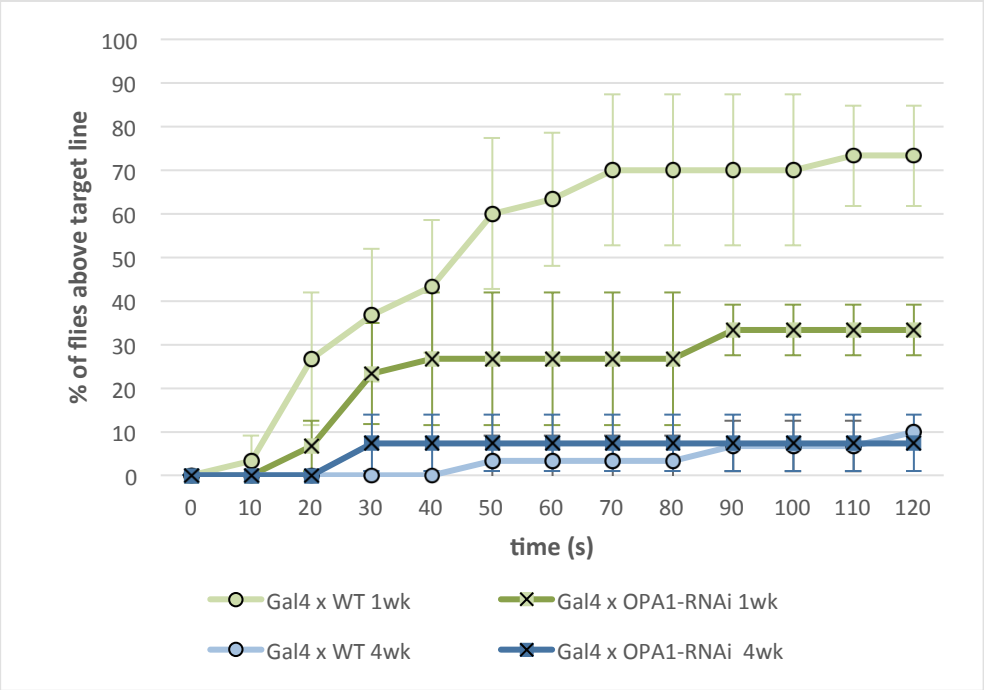
100
90
80
70
60
50
40
30
20
10
0
% of flies above target line
0
10
20
30
40
50
60
70
80
90
100
110
120
time (s)
Gal4 x WT 1wk
Gal4 x OPA1-RNAi 1wk
Gal4 x WT 4wk
Gal4 x OPA1-RNAi 4wk

(b)

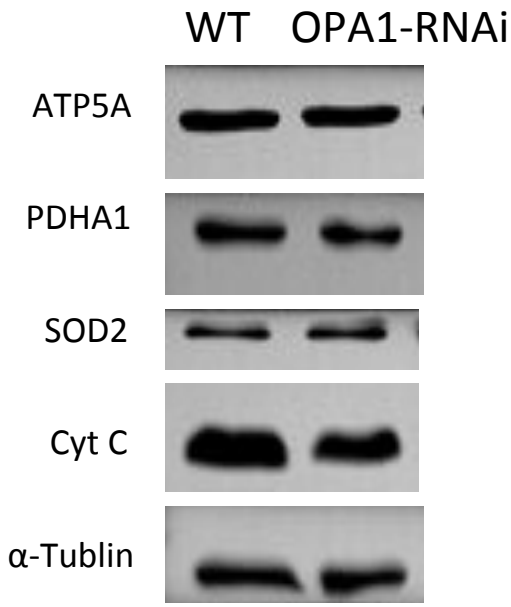
WT
OPA1-RNAi
ATP5A
PDHA1
SOD2
Cyt C
α-Tublin

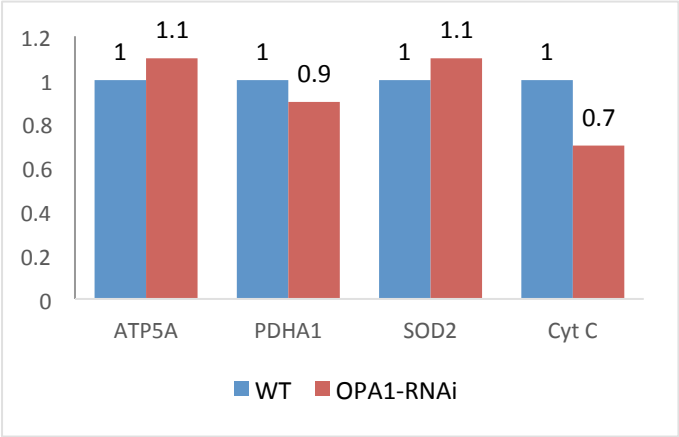
1.2
1
0.8
0.6
0.4
0.2
0
1
1.1
1
0.9
1
1.1
1
0.7
ATP5A
PDHA1
SOD2
Cyt C
WT
OPA1-RNAi

Fig S3

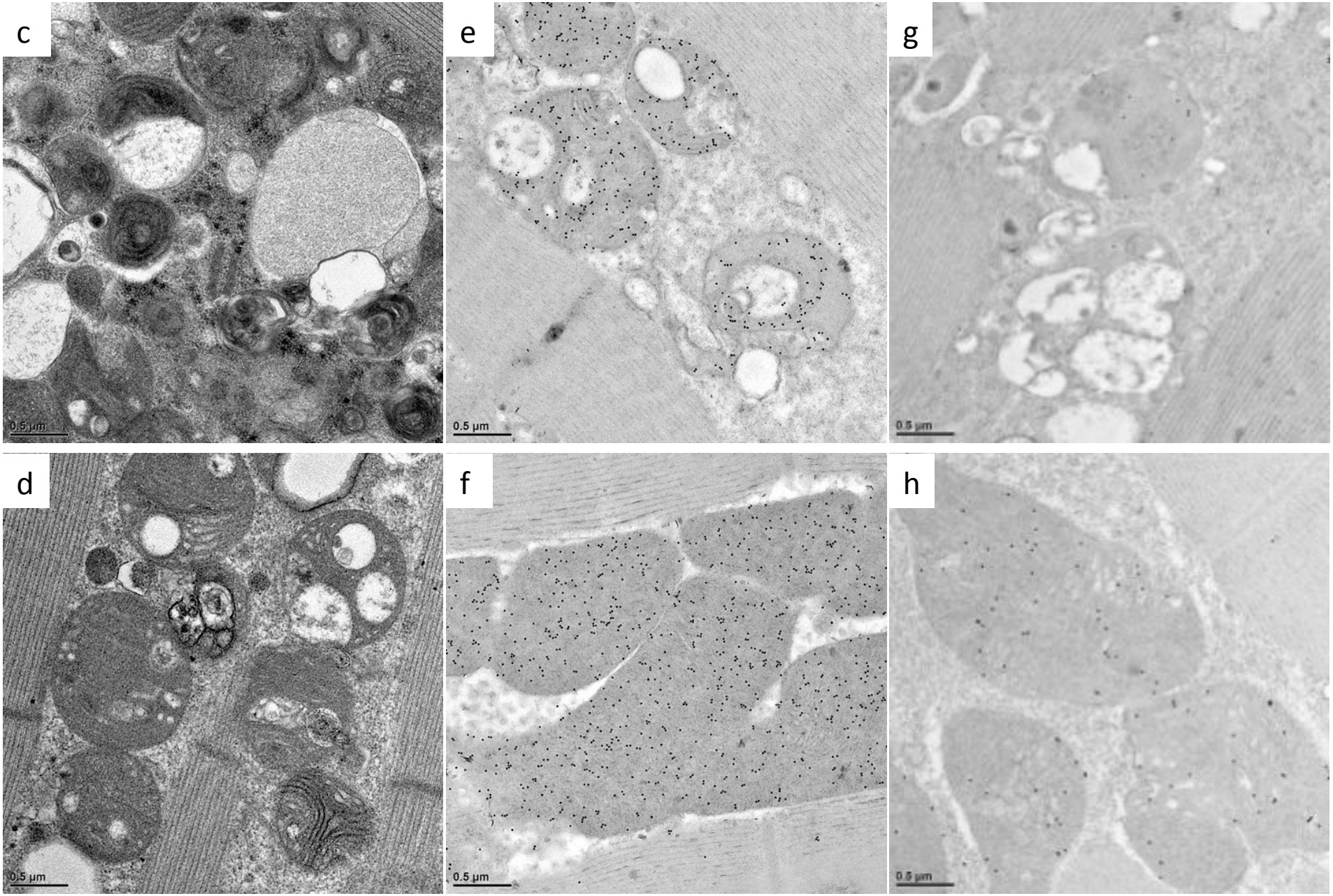

Fig S4

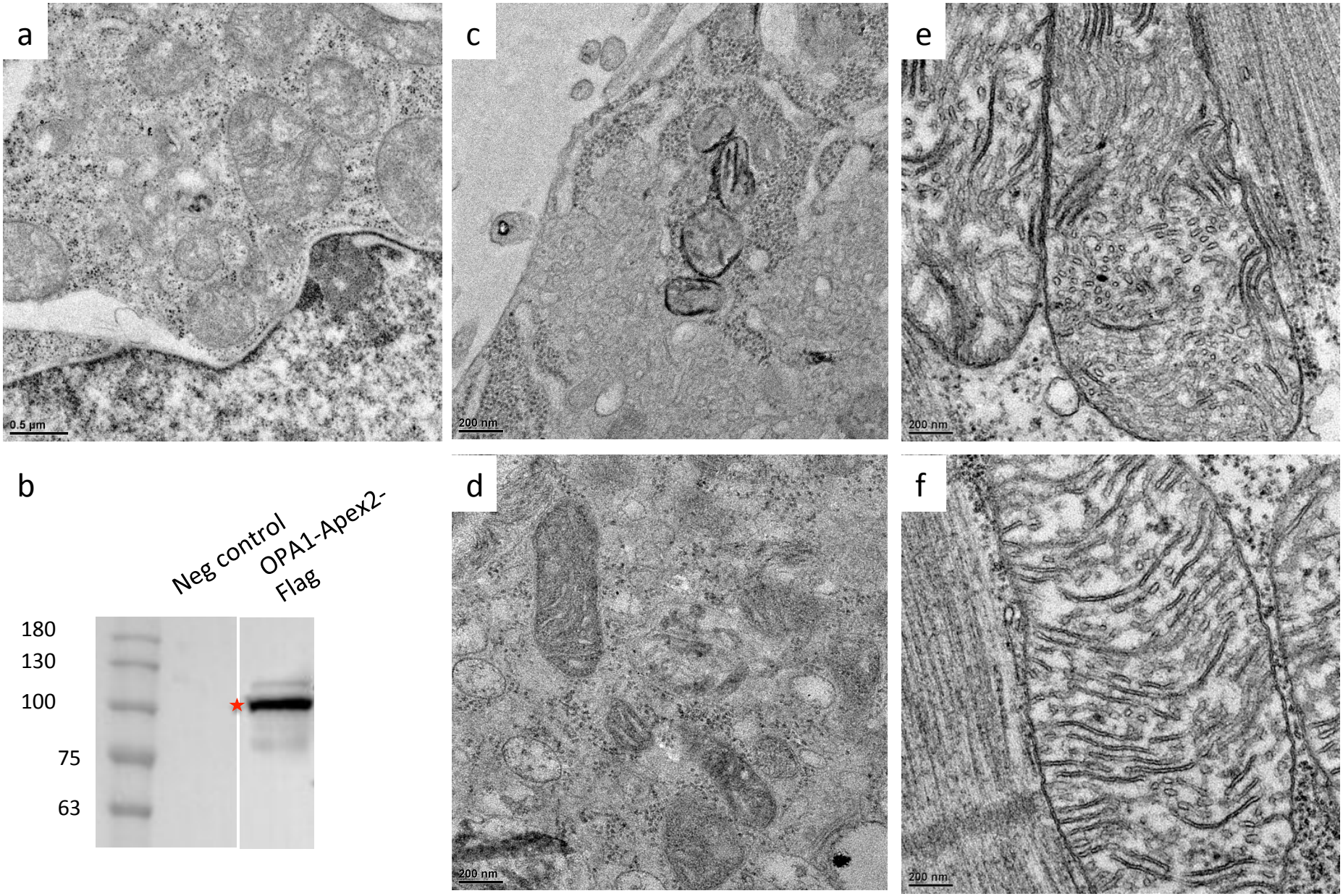
a
0.5 µm
c
200 nm
e
200 nm
b
Neg control
OPA1-Apex2-Flag
180
130
100
75
63
d
200 nm
f
200 nm